Soft Matter

PAPER

View Article Online
View Journal | View Issue

Open Access Article. Published on 10 May 2021. Downloaded on 3/22/2026 4:57:17 PM.
This article is licensed under a Creative Commons Attribution-NonCommercial 3.0 Unported Licence.

Check for updates

Cite this: *Soft Matter*, 2021, **17**, 5384

Controlling line defects in wrinkling: a pathway towards hierarchical wrinkling structures†

André Knapp, *[a] Lisa Julia Nebel, [b] Mirko Nitschke, [c] Oliver Sander [b] and Andreas Fery *[ad]

Received 18th December 2020,
Accepted 19th April 2021

DOI: 10.1039/d0sm02231d

rsc.li/soft-matter-journal

We demonstrate a novel approach for controlling the line defect formation in microscopic wrinkling structures by patterned plasma treatment of elastomeric surfaces. Wrinkles were formed on polydimethylsiloxane (PDMS) surfaces exposed to low-pressure plasma under uniaxial stretching and subsequent relaxation. The wrinkling wavelength λ can be regulated *via* the treatment time and choice of plasma process gases (H_2, N_2). Sequential masking allows for changing these parameters on micron-scale dimensions. Thus, abrupt changes of the wrinkling wavelength become feasible and result in line defects located at the boundary zone between areas of different wavelengths. Wavelengths, morphology, and mechanical properties of the respective areas are investigated by Atomic Force Microscopy and agree quantitatively with predictions of analytical models for wrinkle formation. Notably, the approach allows for the first time the realization of a dramatic wavelength change up to a factor of 7 to control the location of the branching zone. This allows structures with a fixed but also with a strictly alternating branching behavior. The morphology inside the branching zone is compared with finite element methods and shows semi-quantitative agreement. Thus our finding opens new perspectives for "programming" hierarchical wrinkling patterns with potential applications in optics, tribology, and biomimetic structuring of surfaces.

1. Introduction

Wrinkling structures are ubiquitous in nature on different length scales ranging from sub-micron cuticular wrinkles of flower petals to folds with kilometer wavelengths found in geological processes like mountain formation.[1–6] In this paper, we focus on 2-layer systems, where the formation of wrinkles is based on the mechanical mismatch of a thin, stiff film on top of softer bulk material. If in-plane stress is applied, the system reacts by out-off-plane bending of the thin film, and the mechanical mismatch between film and bulk material determines the preferred wavelength/pattern that will arise. The potential of controlled wrinkling for material science has increasingly been recognized during the past 20 years and triggered a copious number of investigations on wrinkle formation in artificial systems. Typically elastomeric materials like polydimethylsiloxane (PDMS) are used as bulk materials, and the thin, stiff film can be formed by various preparation methods,[7–9] *e.g.*, in-situ oxidation with low-pressure plasma, ultraviolet-radiation with ozone (UVO), or wet chemical treatment.[10–12] Thus, wavelengths in artificial wrinkling can be controlled in the range of sub-µm to mm.

However, so far, the complexity of artificial wrinkling structures is far from examples found in biological systems, where distinctive hierarchical structures can be found.[3,5,13,14] In many biological systems, areas of different wavelengths can be encountered instead of a uniform wavelength across the whole surface. Branching of wrinkles is thus a commonly found structural effect. In contrast, wrinkling wavelengths in artificial wrinkling structures are usually constant, and branching often occurs in the form of random line defects at microscopic heterogeneities or due to the wrinkling process getting locked in metastable states, which cannot be controlled.[15–17]

Controlled branching can be facilitated if a lateral change in properties determining the wrinkle wavelength is achieved. Such properties can be film thickness, film stiffness, or substrate stiffness. Vandeparre *et al.* showed the evolution of wrinkles and found line defects in wrinkling patterns.[18] They used a time-dependent decrease of substrate modulus due to a solvent diffusion into titanium sputtered polystyrol sample and thus generated a lateral gradient in the substrate modulus. This resulted in a continuous change of wrinkle amplitude A and wavelength λ. With this diffusion-controlled wrinkling, they

[a] *Institute of Physical Chemistry and Polymer Physics, Leibniz Institute of Polymer Research Dresden e. V., Hohe Str. 6, 01069 Dresden, Germany. E-mail: fery@ipfdd.de; Fax: +49 351 4658 281; Tel: +49 351 4658 225*
[b] *Institute for Numerical Mathematics, Technical University Dresden, Zellescher Weg 12-14, 01069 Dresden, Germany. E-mail: oliver.sander@tu-dresden.de; Tel: +49 351 463 35049*
[c] *Max Bergmann Center of Biomaterials, Leibniz Institute of Polymer Research Dresden e. V., Hohe Str. 6, 01069 Dresden, Germany*
[d] *Chair for Physical Chemistry of Polymeric Materials, Technical University Dresden, Mommsenstr. 4, 01062 Dresden, Germany*

† Electronic supplementary information (ESI) available. See DOI: 10.1039/d0sm02231d

This journal is © The Royal Society of Chemistry 2021

Open Access Article. Published on 10 May 2021. Downloaded on 3/22/2026 4:57:17 PM.
This article is licensed under a Creative Commons Attribution-NonCommercial 3.0 Unported Licence.

fabricated patterns with defined gradual changes in topography, especially regarding λ. These changes show forced line defects as cascade-like Y-branches, which necessarily form as a physical consequence of a growing λ. Further examples of cascade-like patterns consisting of a hierarchy of successive generations of Y-branches were observed in "one-side" compressed free-standing membranes *e.g.* curtains or graphene[19] or in compressed floating thin polymer sheets, where the fluid meniscus follows the contour of the edge of the sheet and reduce the amplitude and wavelength of the wrinkles at the free edge.[20]

Branching as a structuring tool, however, needs a more controlled process with static gradients in the wrinkling-related properties independent of the diffusion time.

Such static gradients can be created by changing the thickness of polymeric or metallic films on top of an elastomeric substrate,[21–23] by changing the substrate stiffness due to asymmetric curing or continuous component shift of a PDMS substrate,[24,25] and by changing both parameters *via* modification of PDMS surface due to plasma/UVO treatment.[26–28] Simulations were carried out by Yin *et al.*[29] for these kinds of gradients. They found Y-branched or multi-branched structures in the case of uniaxial compression perpendicular to a gradient direction, which represent an example of cascade-like branching with randomly located Y-branches.

To use line defects as a structuring tool in a well-defined branching process, such defects need to be controlled and precisely localized. This can be realized by a defined change of the wrinkling parameters perpendicular to the wrinkle direction, which is defined as parallel to the lines of maximum wrinkle amplitude. To quantify the shift in wavelength from one area to the other, we introduce the branching degree as the ratio of wavelengths. Previous investigations used stiffness changes in the substrate[10] or different treatment conditions combined with covered sample areas to achieve changes in wavelength.[25,30–32] These previous approaches are, however, limited in exact localization and controllability of the branching events. Further, the branching degree was limited to a maximum of 1.5. Also, the quality of wrinkled surfaces in the sub-μm range limited a well-defined branching control, primarily through high λ-deviation and randomly distributed line defects.

The local variation of wavelength, localization of defects on the micron-scale, and pronounced changes of wavelength by more than a factor of 2 remain challenging. The present study aims to introduce patterned plasma treatments of PDMS to overcome these limitations and shows a comparison between experimental results on wavelength, morphology and mechanical properties, and analytical/numerical simulation results. This paves the way for predicting branching geometries for this approach. Thus complexity that can be reached in artificial wrinkling structures approaches further to biological examples.

2. Experimental

2.1. PDMS sample preparation

Samples were produced with the two-component system Sylgard 184 (Dow Corning Ltd, Midland, USA). Different component ratios of the base polymer and hardener component were mixed for 2 min and subsequently degassed for 2 min with a Thinky ARE250 tumbling mixer (Thinky Corporation, Tokyo, Japan). Then, the mixtures were molded in Petri dishes and cured for 48 h at room temperature. Two different post-curing steps for 4 h at 80 °C and 48 h at 160 °C were used for different component ratios. Finally, samples of $(45 \times 10 \times 2)$ mm^3 were cut from the cured material.

2.2. Controlled wrinkling process

Samples were clamped in a custom-made polyether-ether-ketone (PEEK) stretching device with an initial length and elongated with 30% strain. PDMS samples were exposed to the plasma treatment in the uniaxially stretched state, and wrinkle formation was triggered by relaxing the samples after the treatment.

2.3. Low-pressure plasma treatment

For plasma treatments of PDMS surfaces a computer-controlled MicroSys apparatus (Roth&Rau, Wüstenbrand, Germany) was used. The cylindrical vacuum chamber, made of stainless steel, has a diameter of 350 mm and a height of 350 mm. The base pressure obtained with a turbomolecular pump is $<10^{-7}$ mbar. On the top of the chamber a 2.46 GHz electron cyclotron resonance plasma source RR160 by Roth & Rau with a diameter of 160 mm and a maximum power of 800 W is mounted. The samples were introduced by a load–lock-system and placed on a grounded holder near the center of the chamber. The distance between the sample and the excitation volume of the plasma source was about 200 mm. The process gas (hydrogen 99.999% or nitrogen 99.999%, Air Liquide) was introduced into the active volume of the plasma source. A process pressure of 2×10^{-2} mbar was adjusted with a gas flow control system. A microwave power of 800 W was used throughout the experiments. To create samples with well-defined lateral gradients of treatment time, a stepper motor-driven retractable shield was placed slightly above the sample surface and removed gradually during plasma exposure. To create samples with an especially sharp edge of the plasma exposed area, silicon masks with a thickness of 150 μm were placed directly on the surface. Successive exposures of the same sample with different process parameters with and without a mask were applied. The treatment time and the process gases were the parameters to control the wrinkling.

2.4. Scanning force microscopy

Topographical analysis of the wrinkled surfaces was done with an atomic force microscope (AFM) (FastScan, Bruker Corporation, Billerica, USA). It was operated in ScanAsyst mode with NanoScope 9.3 software. A FastScan C cantilever (tip radius 5 nm, spring constant 0.8 N m^{-1}, nominal resonance frequency 300 kHz) was used for topographical measurements. The images were taken with a size of (35×35) μm^2 and a resolution of 512×512 pixels. Averaged values and standard deviations for wavelength and amplitude were extracted from AFM data using a self-programmed Python 3.0 Skript (see ESI,† Fig. S1).

Open Access Article. Published on 10 May 2021. Downloaded on 3/22/2026 4:57:17 PM.
This article is licensed under a Creative Commons Attribution-NonCommercial 3.0 Unported Licence.

2.5. Quantitative nanomechanical mapping (QNM)

To determine the mechanical properties of the modified surface of plasma-treated PDMS, cross-section samples were prepared and analyzed. For this, unstrained samples were treated under the same conditions as used in the wrinkling experiments. To increase the adhesive strength, a gas phase silanization of the treated surfaces (vinyltrimethoxysilane, 1 h in a vacuum desiccator under low pressure) was done before a colored embedding overlayer (also Sylgard 184 with an equal component ratio like the treated sample) was cast and cured at room temperature. The three-layer sample (substrate – plasma-treated layer – colored overcast embedding) was cut into smaller pieces (a few mm^3). Smooth polished sections of (100×400) μm^2 perpendicular to the interface were prepared with a cryomicrotome (EM UC6/FC6, Leica, Austria). The QNM measurements were done with an AFM (FastScan, Bruker, USA), operated in ScanAsyst mode with NanoScope 9.3 software and a Fluid+ cantilever (tip radius 5 nm, spring constant 0.7 N m^{-1}). The image size was (1×1) μm^2 with a resolution of 512×512 pixels.

3. Results

First, we investigated the wavelength range accessible by a homogenous treatment of PDMS samples using the process gases N_2 and H_2. The plasma treatment experiments were performed for different substrate Young's moduli.

To get an overview of the different substrate elasticities, the component ratios of Sylgard 184 were changed from 2 : 1 to 20 : 1 (base polymer to hardener component), which allowed the variation of the stiffness in the range between 0.5 and 8 MPa.[33–36] The plasma treatments were performed with N_2 and H_2 for 2 and 4 min with all substrate variations. AFM images of all tested variants are summarized in the ESI† (Fig. S2 and S3). The characterization was carried out regarding the homogeneity of the wrinkled surface, *e.g.*, relating to uncontrolled branching or cracks in the surface. The best homogeneity was found for the component ratio of 2 : 1 (CR2) with post-curing for 4 h at 80 °C, which was then used in further experiments.

Gradient samples were used to determine the possible λ range. They were produced with a retractable shield inside the vacuum chamber, which allowed a plasma exposure with a graded treatment time. Single gradient samples with treatment times of 0 to 480 s were produced. Nitrogen and hydrogen were used as process gases. Using N_2 generates lower absolute wavelengths compared to using H_2, which provides the highest possible absolute wavelengths with the plasma treatment device. Wavelength and the amplitude increased nearly linearly with the given treatment time for both plasma gases. The amplitude was measured as the difference between the minima and maxima of the wrinkles. Fig. 1 summarizes the obtained wavelength and amplitudes for each process gas measured on gradient samples.

N_2 provided a λ range of 444 to 3285 nm. The amplitude ranged from 47 to 865 nm. The λ range is substantially higher for H_2 treatment, and it ranges from 929 to 7364 nm, as well the similar trend was observed regarding the amplitude. The corresponding

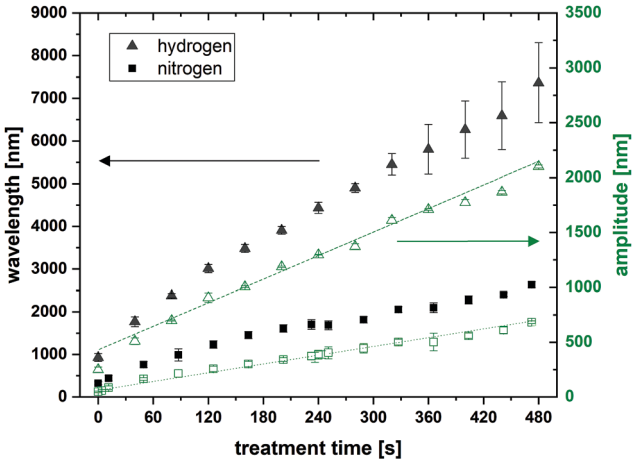

Fig. 1 Treatment time dependence of wavelength (black) and amplitude (green) for plasma process gases N_2 (square) and H_2 (triangle).

amplitude was significantly higher than the amplitude obtained with N_2 and ranged from 250 to 2100 nm.

When a polymer is exposed to a low-pressure plasma a variety of high energy species including vacuum ultraviolet photons but also accelerated ions and neutral molecules contribute to the overall effect. The respective energy distributions, fluxes, and interaction mechanisms determine type, degree, and depth profile of the actual surface modification. For that reason different low pressure plasmas operated with the same excitation but with different process gases are expected to have different interaction profiles with a given organic material. In case of H_2 and N_2 plasma exposure of PDMS this leads to rather different properties of the stiff surface layer. In this study we take advantage of this effect to cover a wavelength range as wide as possible with one and the same low-pressure plasma device.

The wavelength calculations with the analytical eqn (1) and (2)[37] were used to verify the experimental results and provide a benchmark for further finite element simulations.

$$\lambda = 2\pi h_f \left(\frac{E_f(1-\nu_s^2)}{3E_S(1-\nu_f^2)} \right)^{(1/3)} \tag{1}$$

$$\lambda_{calc} = \frac{\lambda}{(1+\varepsilon)\left(1+\frac{5\varepsilon(1+\varepsilon)}{32}\right)^{(1/3)}} \tag{2}$$

The λ as determined by eqn (1) depends on the film thickness h_f, Young's modulus of the film E_f and the substrate E_S, the Poission ratios of the film ν_f and the substrate ν_S, as well as the applied uniaxial strain ε. The empirical eqn (2) reduced the deviations due to the higher used pre-strain compared to the critical strain, where ε represents the applied pre-strain reported in the experimental section. To test this hypothesis, flat N_2 – plasma treated and wrinkled samples were used. All these parameters were measured by tensile tests and QNM (Fig. S5 and S6, ESI†) and summarized in Table 1.

The well-known analytical eqn (1) and (2) are valid for a bi-layer. The consequence is, that the exponential stiffness decrease into

Open Access Article. Published on 10 May 2021. Downloaded on 3/22/2026 4:57:17 PM.
This article is licensed under a Creative Commons Attribution-NonCommercial 3.0 Unported Licence.

Table 1 Material parameters and comparison of measured and calculated wavelengths for N_2 plasma treatment: h_f represents the film thickness from 25% increase of the measured stiffness to the stiffness maxima, E_f the mean stiffness in the range of this thickness, λ_{calc} the calculated wavelengths and λ_{topo} the measured wavelength (substrate stiffness was E_S = 0.76 MPa for all samples and depended only on the component ratio CR2, Poisson ratios for the substrate and the film were 0.5 and 0.33, respectively)

Time [s]	h_f [nm]	E_f [MPa]	λ_{calc} [nm]	λ_{topo} [nm]
30	128 ± 23	11.3	978 ± 218	624 ± 69
60	143 ± 22	12.1	1115 ± 199	831 ± 76
120	133 ± 5	20.4	1217 ± 67	1289 ± 96
240	255 ± 33	13.9	2043 ± 376	1983 ± 56

the substrate material had to be averaged to get such a bi-layer like model, represented by the film thickness h_f and a step like constant mean film stiffness E_f. This approximation was done by mean calculation of the stiffness in the range of the measured thickness. This leads to the effect that the film stiffness E_f passes through an ostensible maximum, what is only a consequence of the average process and does not represent an absolute stiffness maximum. The thickness increases continuously with treatment time within the experimental error bars.

The wavelength of the wrinkle pattern for different plasma treatments was compared by two independent approaches: (a) directly measured with topographical AFM images (λ_{topo}) and (b) indirectly calculated from QNM cross-section analysis *via* E_f and h_f (λ_{calc}). The calculation using eqn (1) and (2) approximates the complex depth profile of Young's modulus (see Fig. S5 and S6, ESI†) with the simple bi-layer model. This requires an averaging procedure to determine E_f which is less or more appropriate depending on the actual shape of the modulus profile. In the particular case of the presented data the procedure provides more reliable results for longer treatment times. The data on effective modulus and thickness of the modified layers show that both parameters do not exhibit a simple proportionality to the treatment time, which is not surprising due to the complex processes involved. To the best of our knowledge, there is no physical model which explains the linear trend of wavelength with treatment time. This finding will be subject to further studies which go beyond the current report. But nevertheless, the comparison showed reasonable accordance between the directly measured and indirectly calculated wavelengths, but also the limitation of the analytical equations to approximate the experimentally observed dependency of the wavelength shown in Fig. 1, especially for low treatment times.

3.1. Controlled branching with a masking technique

Fig. 2 illustrates the masking technique used to obtain localized wrinkles. A strained substrate covered with a mask was treated with plasma. With this 1st treatment, only the unmasked area was modified. The mask was removed, and the 2nd plasma treatment step was carried out on the still strained substrate without the mask. This way, sharply separated areas with different film properties were produced, where the areas treated twice lead to λ like in cumulated single treatment steps using the same treatment time. The strain was finally released to get wrinkles on the substrate.

Masks with a thickness as low as possible are required for this purpose. The reason for this is a penumbra effect at the mask edge that occurs for any directed component of the complex plasma impact due to the given exposure geometry (source diameter 160 mm).

To quantify the mechanical changes induced by the plasma treatment as well as to quantify the sharpness of the transition zone, unstrained masked samples were treated for 4 min with N_2 plasma. To evaluate the transition zone, the surface stiffness in the transition area was measured with QNM. Fig. 3 shows a measured stiffness map of the transition zone between the treated and untreated areas. The determination provided a stiffness transition zone of (630 ± 188) nm for N_2 plasma. The measured transition zone is smaller than the minimum

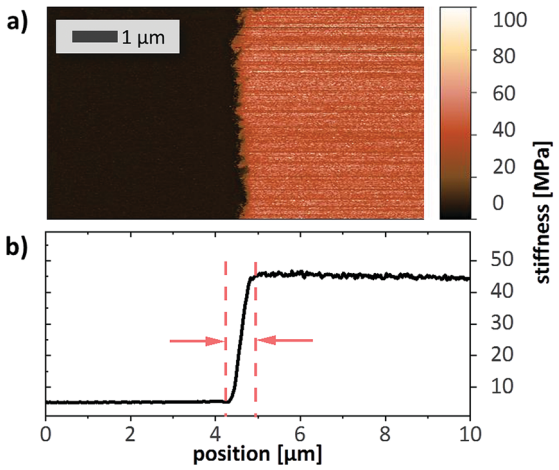

Fig. 3 (a) Topographic image with measured stiffness step and width of the transition zone between treated (light orange) and untreated area (dark orange) for a 2 : 1 PMDS and N_2 plasma treatment with AFM; (b) average stiffness profile with transition zone width.

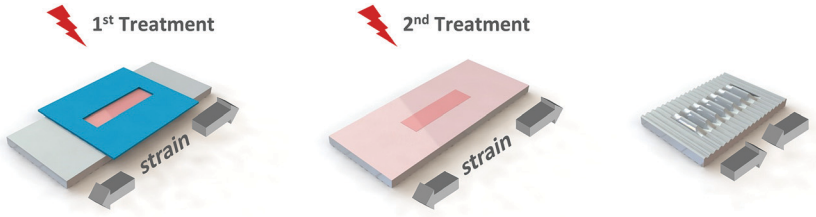

Fig. 2 Schematic illustration of the masked wrinkling process.

Open Access Article. Published on 10 May 2021. Downloaded on 3/22/2026 4:57:17 PM.
This article is licensed under a Creative Commons Attribution-NonCommercial 3.0 Unported Licence.

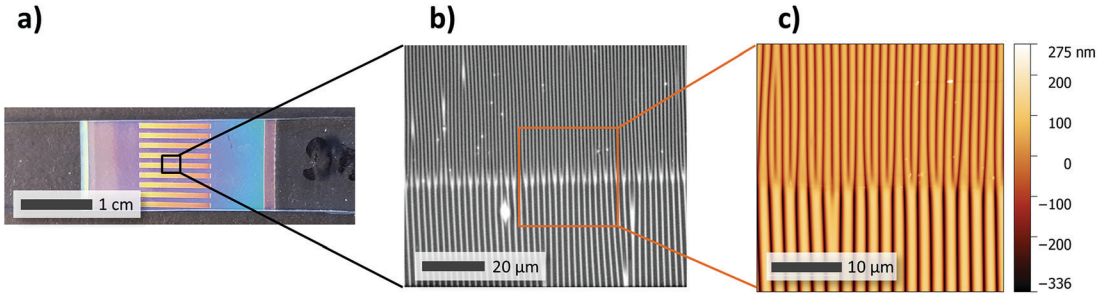

Fig. 4 (a) Photograph of a sample with clearly visible areas of different wavelengths, the yellow stripes represent the areas with a high λ, the surrounding area shows lower λ; (b) 50× magnified microscopy image of localized line defects along different λ-areas; (c) topographic image measured with AFM for detailed characterization of λ, amplitude, and branching degree.

wavelength for both process gases, which is about 800 nm for N_2 plasma treatment.

With this masking technique, location-independent combinations of plasma treatment parameters like time variation and process gas are possible. This allows the combination of process conditions leading to different wavelengths and enabling the possibility of high wavelength-differences, high branching degrees, and consequently a controlled branching process of surface wrinkles. Fig. 4 shows an example of controlled localized branching. The photograph in Fig. 4a illustrates the typical angle-dependent reflection colors of wrinkled surfaces caused by interference. Differences in structural colors correspond to regions of different wavelengths. The homogeneous color of the strips and the surrounding area gives a first impression of the homogeneity of the produced wrinkles. The microscopy image in Fig. 4b with a magnification factor of 50× allows resolving the individual wrinkles and the transition zone. The wrinkles of the bigger wavelength split into wrinkles with smaller λ exactly along the line representing the mask edge. The different λ areas are homogeneous over a large area (90 µm × 76 µm). Fig. 4c shows an AFM image, which allows the quantification of wavelength, amplitude, and branching. The branching degree as a consequence of the wavelength change and the amplitude transition from one area to a neighboring one can be investigated. It is visible that the branching zone is not affected by the transition zone we described before. The branching events were localized along a line with dislocations smaller than 1 µm.

3.2. Variation of branching degree

The evaluation of the range of branching degrees (BD) was done with the plasma gases N_2, H_2, and their combination with CR2 substrate material for different base wavelengths. First, we started with N_2 plasma gas and the highest reachable λ of 3000 nm as base wavelength. With this choice, it was possible to produce BDs of up to 3, *i.e.*, one large wrinkle splitting into three smaller ones. Homogenous branching with different branching degrees (2 or 3) as well as all intermediate BDs with alternating branching behavior (*e.g.* 1.5 or 2.5) was possible. To push for extreme BD, a high difference between used wavelengths was necessary. This was shown with an 800 nm base wavelength that produced a BD up to 3.5. The second tested plasma gas was H_2. The absolute higher wavelength enabled the branching in a different λ-range from 1000 nm up to 7000 nm, where a 2000 nm base λ was used for the practical test. With these higher absolute wavelengths, branching degrees up to 4 could be realized, but also all intermediate BD with homogenous and alternating branching behavior. Detailed results are summarized in ESI,† Fig. S4. The sharply localized stiffness steps in combination with transition zones in the range of the used wavelengths between the wrinkled areas suppressed an evolutional cascade branching over a large distance known from the literature.[19,20] When looking at the transition between different wrinkle modes, we can distinguish between a smooth change in stress over the whole transition zone or a focused stress region. The masking process in our experiments results in a very narrow transition zone, leading to a focused stress region. As discussed in Schroll *et al.*, a focused stress region is a cause for an abrupt change in the wrinkle height, therefore we see transitions with minimized cascades.[38] This does not mean, that minimal evolutional cascades are might not be present, but then they are very localized such that the branching starts nearly simultaneous.

In practice, the reached branching degree for single plasma gases shows that the useable λ range enables BDs of up to 4, but not higher. The limiting factors for N_2 are the randomly located line defects with low λ and of course the maximal reachable λ. The used two-step masking process allows the combination of different plasma gases to combine the specific reachable λ ranges of the single plasma gases. To produce BDs higher than 4 a combination of H_2 and N_2 was used. First, the substrate was treated with H_2 to reach a λ above the maximum λ for N_2 plasma, followed by a second treatment-step with N_2 plasma to get a λ below the minimum λ for H_2. This process used different process gases for the masked and unmasked treatment steps and led to an area treated twice (H_2 + N_2) with a resulted λ of 5650 nm, whereas the area treated with only one process gas (N_2) led to a λ of 850 nm. In this way, the BD could be increased to up to 7. The described sharp localized stiffness steps in combination with transition zones in the range of the used wavelengths, suppressed a cascade-like branching like by the treatment with single-process gases. The branching started immediately and without clear visible cascade branching (see ESI,† Fig. S7).

Fig. 5 gives an overview of branching scenarios depending on the process gases or the combinations thereof.

 This journal is © The Royal Society of Chemistry 2021

Open Access Article. Published on 10 May 2021. Downloaded on 3/22/2026 4:57:17 PM.
This article is licensed under a Creative Commons Attribution-NonCommercial 3.0 Unported Licence.

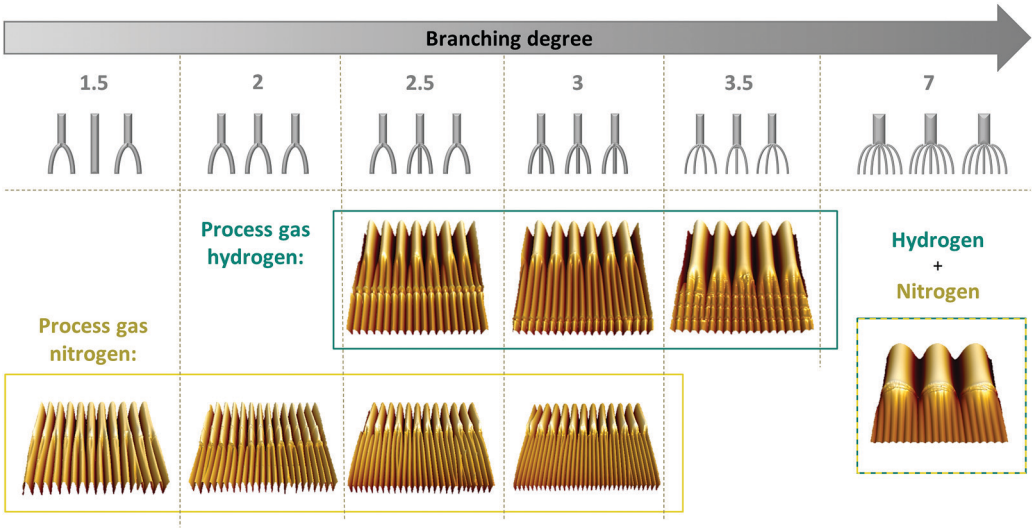

Fig. 5 Branching scenarios sorted by branching degree for the process gases N_2, H_2, and their combinations, produced with the masking technique and measured with AFM.

High-quality N_2 branching without randomly localized line defects was successful in the wavelength range from 1000–3000 nm and enabled, BDs up to 3. H_2 branching was possible in the λ range from 2000–7000 nm and enabled BDs up to 3.5. In principle, every process gas enables BDs of around 1 up to 3–4 in their specific absolute λ range. Higher BDs up to 7 and more could be obtained with a combination of the process gases.

4. Finite element simulations

While analytical solutions are possible in some simple cases of homogeneous wrinkling, the complex scenarios encountered in these experiments require numerical simulations. The wavelength and amplitude changes in the branching area are an essential point of interest for comparing the experimental results and simulations.

We model the substrate as a rectangular block of dimensions 60 μm in x-direction, 20 μm in y-direction and 20 μm in z-direction. We stretch it uniaxially in x-direction by 30% using displacement boundary conditions on one side while fixing the rectangular block on the opposite side using Dirichlet boundary conditions. We use a Mooney–Rivlin material[33] with parameters derived from uniaxial tensile tests (Table S1, ESI†). On the deformed upper surface, we then attach a stiffer material layer modeled by a geometrically exact Cosserat shell as described in ref. 39. The material parameters are summarized in Table S2 (ESI†). While the shell model is two-dimensional, the thickness h appears as a material parameter. This thickness parameter and the stiffness parameters μ_{stiff} and λ_{stiff}, which determine the elastic behavior of the Cosserat shell, take position-dependent values. This allows us to simulate the masking process described above. These changes in parameters trigger the wrinkle branching behavior. We release the uniaxial component of the displacement boundary conditions, thus releasing the 30% stretch, and observe how wrinkling patterns form due to the stress mismatch of substrate and stiff layer.

The calculations were done using the DUNE libraries for C++ for solving partial differential equations (PDEs) with grid-based methods.[40] We discretize the model using second-order (27-nodes) Lagrange finite elements for the substrate, and second-order (9-nodes) geodesic finite elements for the shell.[41] As shown experimentally in ref. 42, no locking occurs for this type of shell discretization. We start with a cubical grid for the substrate which is then manually graded resulting in a hierarchical grid with a high resolution in the vicinity of the shell. In total, the substrate grid has 15 642 vertices. The attached shell model is discretized on the two-dimensional restriction of the substrate grid to the upper boundary in y-direction, which has 3993 vertices. This setup results in a nonlinear minimization problem which we solve using a trust-region method, an iterative method considering a linearized version of the problem in each step. As an experimental reference sample and base for the material characterization, we used a branching case that was realized by treatment with N_2 plasma for 60 s and 240 s. To trigger branching of the wrinkling pattern, we divided the shell horizontally into two halves in strain direction. We assigned thickness parameters h_1 = 238.5 μm in the upper half and h_2 = 142.5 μm in the lower half, and elastic moduli of E_1 = 13.87 MPa in the lower half and E_2 = 12.14 MPa in the upper half. These parameters were measured with QNM cross-section measurement (Fig. S5, ESI†) for known wrinkle patterns and their corresponding thickness and stiffness values (Fig. S6, ESI†). Simulation results and the corresponding experiments are shown in Fig. 6.

The wavelengths resulting from the numerical simulations are (994 ± 136) nm for the upper half and (1932 ± 184) nm for the lower half calculated with the same Python script as we used for the experiments. The corresponding experimental wavelengths are (831 ± 77) nm and (1983 ± 56) nm, respectively. These results are closer to the experiments than the results of the analytical equations (Table 1), especially for low wavelengths. The ratio of the number of wrinkles resulting from

Open Access Article. Published on 10 May 2021. Downloaded on 3/22/2026 4:57:17 PM.
This article is licensed under a Creative Commons Attribution-NonCommercial 3.0 Unported Licence.

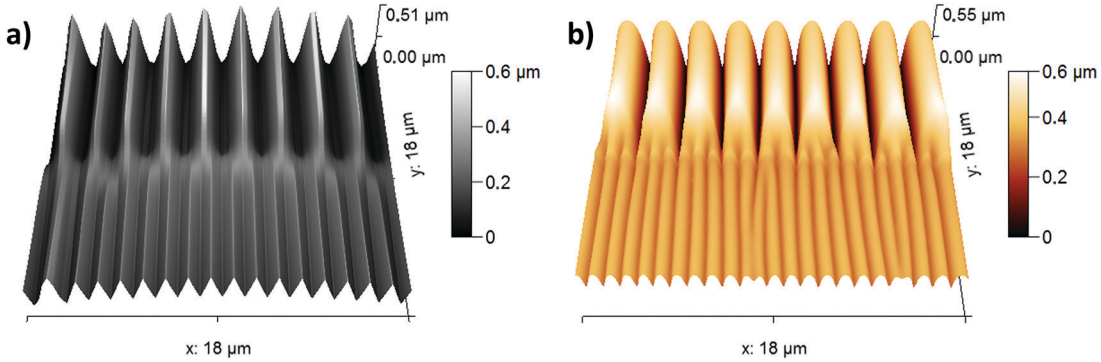

Fig. 6 (a) Simulation result of wrinkle patterns with two different wavelengths and the branching zone between them as a topographic image (b) Experimental wrinkle pattern with the same mechanical properties (in both images, color represents the elevation).

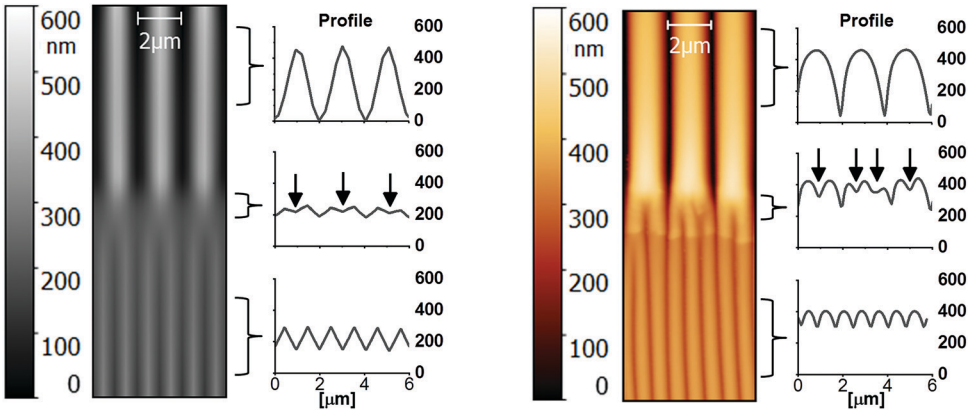

Fig. 7 Comparison of experimental branched wrinkle (right) shape with simulation outcome (left) (arrows represent the new minima, where the wrinkle splits into smaller ones).

the simulation is 1.94, which is close to the wrinkle ratio of 2.37 of the corresponding experimental results. The resulting amplitudes are (120 ± 25) nm for the upper half and (354 ± 46) nm for the lower half, compared with experimental results of (101 ± 10) nm and (416 ± 40) nm, respectively.

The localization of line defects for the branching occurs in the transition zone between the adjacent wrinkling areas. The correspondent adjustment of the amplitude, induced by the change of wrinkle shape in the branching zone, depends on the branching degree. This behavior can be observed both in the experimental and in the simulation results (Fig. 7). The wrinkle shape transition starts with a high wavelength and amplitude; then branching occurs when large wrinkles split into smaller ones, *i.e.*, each wrinkle maximum splits into local maxima with a new small minimum developing between them. The new small minimum increases while the initial wrinkle minimum decreases. This transition process ends as soon as the small wavelength and the corresponding amplitude are fully reached.

The experimental wrinkle shapes differ from the simulated ones for several reasons. The used grid size in the simulation resulted in a more triangular wrinkle shape compared to the more sinusoidal shape in the experiment. Further, the symmetry break in the wrinkle shape was more pronounced in the experiment than in the simulation results. This asymmetric wrinkle shape depends on the ratio of film and substrate stiffness as well as the used substrate pre-stretch.[43] In the experiment we can see V-shaped minima in contrast to more sinusoidal maxima.

5. Conclusions

We show a novel method to generate highly localized and hierarchical wrinkling structures. We combine multi-step low-pressure plasma treatment with masking of elastomeric PDMS samples, creating a modified PDMS surface with areas of different film thickness and stiffness. Importantly, and in contrast to earlier work, we find very sharp transition zones between the areas (on the order of less than 1 micrometer). The process gases (H_2 and N_2) and preparation conditions allow accessing an extensive range of wavelengths (between 444 nm and 7364 nm), spanning more than one order of magnitude. Since, at the same time, the transition zone is not larger than the wrinkling wavelength, the system shows very abrupt wavelength changes. This causes line defects to be effectively pinned in the transition zone. While previous reports only show changes up to wavelength doubling, we can access a regime up to seven-fold change of wavelength and still observe clear branching features rather than rupture between the mechanically mismatching areas.

 This journal is © The Royal Society of Chemistry 2021

Open Access Article. Published on 10 May 2021. Downloaded on 3/22/2026 4:57:17 PM.
This article is licensed under a Creative Commons Attribution-NonCommercial 3.0 Unported Licence.

We were able to semi-quantitatively reproduce the wrinkling behavior in a finite element simulation using a geometrically exact Cosserat shell on a hyperelastic Mooney–Rivlin-substrate, which shows perspectives for the future rational design of intricate wrinkling patterns.

Hierarchical wrinkling offers a range of perspectives. First, wrinkles are well known to influence optical, wetting, and tribological properties as well as the interaction with biological systems.[44–47] Surfaces featuring different wrinkle wavelength and amplitude allow combinatorial approaches for investigating these effects. As well, the combination of different wrinkled surfaces (*e.g.*, the effect of wrinkles on friction, capillary forces, and adhesion[48,49]) can thus be efficiently screened. Second, the branching points themselves are of interest as symmetry-breaking elements, which could, for example, serve as optical vertices or allow for selective deposition of nanoparticles at branching points, to mention just a few perspectives.

Data availability

The raw data can be provided on request.

Conflicts of interest

The authors declare no competing financial interest. There are no conflicts to declare.

Acknowledgements

We thank B. Glatz for preliminary work, as well as U. Reuter and A. Janke for assistance in AFM sample preparation. This work was funded by the DFG FE 600/20-1 640690 project.

References

1 P. Yamato, B. J. P. Kaus, F. Mouthereau and S. Castelltort, Dynamic constraints on the crustal-scale rheology of the Zagros fold belt, Iran, *Geology*, 2011, **39**, 815–818.
2 S. Kondo and R. Asai, A reaction–diffusion wave on the skin of the marine angelfish Pomacanthus, *Nature*, 1995, **376**, 765–768.
3 D. Voigt, A. Schweikart, A. Fery and S. Gorb, Leaf beetle attachment on wrinkles: isotropic friction on anisotropic surfaces, *J. Exp. Biol.*, 2012, **215**, 1975–1982.
4 M. J. Baum, L. Heepe and S. N. Gorb, Friction behavior of a microstructured polymer surface inspired by snake skin, *Beilstein J. Nanotechnol.*, 2014, **5**, 83–97.
5 B. Prüm, H. Florian Bohn, R. Seidel, S. Rubach and T. Speck, Plant surfaces with cuticular folds and their replicas: Influence of microstructuring and surface chemistry on the attachment of a leaf beetle, *Acta Biomater.*, 2013, **9**, 6360–6368.
6 M. Holland, S. Budday, A. Goriely and E. Kuhl, Symmetry Breaking in Wrinkling Patterns: Gyri Are Universally Thicker than Sulci, *Phys. Rev. Lett.*, 2018, **121**, 228002.
7 N. B. Bowden, W. T. S. Huck, K. E. Paul and G. M. Whitesides, The Controlled Formation of Ordered, Sinusoidal Structures by Plasma Oxidation of an Elastomeric Polymer, *Appl. Phys. Lett.*, 1999, **75**, 2557–2559.
8 A. Schweikart and A. Fery, *Controlled wrinkling as a novel method for the fabrication of patterned surfaces*, 2009, vol. 165.
9 Q. Wang and X. Zhao, A three-dimensional phase diagram of growth-induced surface instabilities, *Sci. Rep.*, 2015, **5**, 8887.
10 B. A. Glatz, M. Tebbe, B. Kaoui, R. Aichele, C. Kuttner, A. E. Schedl, H. W. Schmidt, W. Zimmermann and A. Fery, Hierarchical line-defect patterns in wrinkled surfaces, *Soft Matter*, 2015, **11**, 3332–3339.
11 B. Glatz and A. Fery, *The influence of plasma treatment on the elasticity of the in situ oxidized gradient layer in PDMS: towards crack-free wrinkling*, 2018, vol. 15.
12 M. Watanabe and K. Mizukami, Well-Ordered Wrinkling Patterns on Chemically Oxidized Poly(dimethylsiloxane) Surfaces, *Macromolecules*, 2012, **45**, 7128–7134.
13 P. Rofouie, D. Pasini and A. D. Rey, Tunable nano-wrinkling of chiral surfaces: Structure and diffraction optics, *J. Chem. Phys.*, 2015, **143**, 114701.
14 P. Rofouie, D. Pasini and A. D. Rey, Multiple-wavelength surface patterns in models of biological chiral liquid crystal membranes, *Soft Matter*, 2017, **13**, 541–545.
15 K. Efimenko, M. Rackaitis, E. Manias, A. Vaziri, L. Mahadevan and J. Genzer, Nested self-similar wrinkling patterns in skins, *Nat. Mater.*, 2005, **4**, 293–297.
16 J. W. Hutchinson and X. Chen, Herringbone Buckling Patterns of Compressed Thin Films on Compliant Substrates, *J. Appl. Mech.*, 2004, **71–75**, 597–603.
17 Y. Ni, D. Yang and L. He, Spontaneous wrinkle branching by gradient stiffness, *Phys. Rev. E: Stat., Nonlinear, Soft Matter Phys.*, 2012, **86**, 031604.
18 H. Vandeparre, S. Gabriele, F. Brau, C. Gay, K. K. Parker and P. Damman, Hierarchical wrinkling patterns, *Soft Matter*, 2010, **6**, 5751.
19 H. Vandeparre, M. Piñeirua, F. Brau, B. Roman, J. Bico, C. Gay, W. Bao, C. N. Lau, P. M. Reis and P. Damman, Wrinkling Hierarchy in Constrained Thin Sheets from Suspended Graphene to Curtains, *Phys. Rev. Lett.*, 2011, **106**, 224301.
20 J. Huang, B. Davidovitch, C. D. Santangelo, T. P. Russell and N. Menon, Smooth Cascade of Wrinkles at the Edge of a Floating Elastic Film, *Phys. Rev. Lett.*, 2010, **105**, 038302.
21 G. Miquelard-Garnier, A. B. Croll, C. S. Davis and A. J. Crosby, Contact-line mechanics for pattern control, *Soft Matter*, 2010, **6**, 5789–5794.
22 S.-J. Yu, Y. Ni, L. He and Q. Ye, Tunable Formation of Ordered Wrinkles in Metal Films with Controlled Thickness Gradients Deposited on Soft Elastic Substrates, *ACS Appl. Mater. Interfaces*, 2015, **7**(9), 5160–5167.
23 J. Schleifer, J. Marthelot, T. J. Jones and P. T. Brun, The fingerprint of a flow: wrinkle patterns in nonuniform coatings on pre-stretched soft foundations, *Soft Matter*, 2019, **15**, 1405–1412.
24 V. Parihar, S. Bandyopadhyay, S. Das, R. Mukherjee, S. Chakraborty and S. Dasgupta, Tailored topography: a

Open Access Article. Published on 10 May 2021. Downloaded on 3/22/2026 4:57:17 PM.
This article is licensed under a Creative Commons Attribution-NonCommercial 3.0 Unported Licence.

novel fabrication technique using an elasticity gradient, *Soft Matter*, 2018, **14**, 7034–7044.

25 K. U. Claussen, M. Tebbe, R. Giesa, A. Schweikart, A. Fery and H.-W. Schmidt, Towards tailored topography: facile preparation of surface-wrinkled gradient poly(dimethyl siloxane) with continuously changing wavelength, *RSC Adv.*, 2012, **2**, 10185–10188.

26 E. P. Chan and A. J. Crosby, Spontaneous formation of stable aligned wrinkling patterns, *Soft Matter*, 2006, **2**, 324–328.

27 H. Li, B. Sheng, H. Wu, Y. Huang, D. Zhang and S. Zhuang, Ring Wrinkle Patterns with Continuously Changing Wavelength Produced Using a Controlled-Gradient Light Field, *Materials*, 2018, **11**(9), 1571.

28 Q. Zhou, P. T. Kühn, T. Huisman, E. Nieboer, C. van Zwol, T. G. van Kooten and P. van Rijn, Directional nanotopographic gradients: a high-throughput screening platform for cell contact guidance, *Sci. Rep.*, 2015, **5**, 16240.

29 J. Yin and X. Chen, Elastic buckling of gradient thin films on compliant substrates, *Philos. Mag. Lett.*, 2010, **90**, 423–433.

30 B. Kaoui, A. Guckenberger, A. Krekhov, F. Ziebert and W. Zimmermann, Coexistence of stable branched patterns in anisotropic inhomogeneous systems, *New J. Phys.*, 2015, **17**, 103015.

31 D. Rhee, J. T. Paci, S. Deng, W.-K. Lee, G. C. Schatz and T. W. Odom, Soft Skin Layers Enable Area-Specific, Multiscale Graphene Wrinkles with Switchable Orientations, *ACS Nano*, 2020, **14**, 166–174.

32 S. Hiltl and A. Böker, Wetting Phenomena on (Gradient) Wrinkle Substrates, *Langmuir*, 2016, **32**, 8882–8888.

33 R. Seghir and S. Arscott, Extended PDMS stiffness range for flexible systems, *Sens. Actuators, A*, 2015, **230**, 33–39.

34 I. D. Johnston, D. K. McCluskey, C. K. L. Tan and M. C. Tracey, Mechanical characterization of bulk Sylgard 184 for microfluidics and microengineering, *J. Micromech. Microeng.*, 2014, **24**, 035017.

35 K. Khanafer, A. Duprey, M. Schlicht and R. Berguer, Effects of strain rate, mixing ratio, and stress-strain definition on the mechanical behavior of the polydimethylsiloxane (PDMS) material as related to its biological applications, *Biomed. Microdevices*, 2009, **11**, 503–508.

36 A. Lamberti, M. Di Donato, A. Chiappone, F. Giorgis and G. Canavese, Tunable electromechanical actuation in silicone dielectric film, *Smart Mater. Struct.*, 2014, **23**, 105001.

37 H. Jiang, D. Y. Khang, J. Song, Y. Sun, Y. Huang and J. A. Rogers, Finite deformation mechanics in buckled thin films on compliant supports, *Proc. Natl. Acad. Sci. U. S. A.*, 2007, **104**, 15607–15612.

38 R. D. Schroll, E. Katifori and B. Davidovitch, Elastic Building Blocks for Confined Sheets, *Phys. Rev. Lett.*, 2011, **106**, 074301.

39 M. Bîrsan, I.-D. Ghiba, R. J. Martin and P. Neff, Refined dimensional reduction for isotropic elastic Cosserat shells with initial curvature, *Math. Mech. Solids*, 2019, **24**, 4000–4019.

40 P. Bastian, M. Blatt, A. Dedner, C. Engwer, R. Klöfkorn, M. Ohlberger and O. Sander, A generic grid interface for parallel and adaptive scientific computing. Part I: abstract framework, *Computing*, 2008, **82**, 103–119.

41 O. Sander, Geodesic finite elements of higher order, *IMA J. Numer. Anal.*, 2015, **36**, 238–266.

42 O. Sander, P. Neff and M. Bîrsan, Numerical treatment of a geometrically nonlinear planar Cosserat shell model, *Comput. Mech.*, 2016, **57**, 817–841.

43 J. W. Hutchinson, The role of nonlinear substrate elasticity in the wrinkling of thin films, *Philos. Trans. R. Soc., A*, 2013, **371**, 20120422.

44 P.-C. Lin and S. Yang, Mechanically switchable wetting on wrinkled elastomers with dual-scale roughness, *Soft Matter*, 2009, **5**, 1011–1018.

45 H. Wu, S. Yu, Z. Xu, B. Cao, X. Peng, Z. Zhang, G. Chai and A. Liu, Theoretical and Experimental Study of Reversible and Stable Wetting States of a Hierarchically Wrinkled Surface Tuned by Mechanical Strain, *Langmuir*, 2019, **35**, 6870–6877.

46 P. T. Probst, S. Sekar, T. A. F. Konig, P. Formanek, G. Decher, A. Fery and M. Pauly, Highly Oriented Nanowire Thin Films with Anisotropic Optical Properties Driven by the Simultaneous Influence of Surface Templating and Shear Forces, *ACS Appl. Mater. Interfaces*, 2018, **10**, 3046–3057.

47 Y. Sun, K. Wu, Y. Wang, J. Zhang, G. Liu and J. Sun, Controlled wrinkling patterns and surface friction by thickness gradient, *Surf. Coat. Technol.*, 2020, **401**, 126279.

48 C.-H. Lin, C.-Y. Huang, J.-Y. Ho and H.-Y. Hsueh, Symmetrical Wrinkles in Single-Component Elastomers with Fingerprint-Inspired Robust Isotropic Dry Adhesive Capabilities, *ACS Appl. Mater. Interfaces*, 2020, **12**(19), 22365–22377.

49 H. Monobe, T. Ohzono, H. Akiyama, K. Sumaru and Y. Shimizu, Manipulation of Liquid Filaments on Photoresponsive Microwrinkles, *ACS Appl. Mater. Interfaces*, 2012, **4**, 2212–2217.

 This journal is © The Royal Society of Chemistry 2021